

# Introducing a strain-hardening capability to improve the ductility of bulk metallic glasses via severe plastic deformation

Y.B. Wang<sup>a</sup>, D.D. Qu<sup>b</sup>, X.H. Wang<sup>a</sup>, Y. Cao<sup>a</sup>, X.Z. Liao<sup>a,\*</sup>, M. Kawasaki<sup>c</sup>, S.P. Ringer<sup>d</sup>, Z.W. Shan<sup>e</sup>, T.G. Langdon<sup>c,f</sup>, J. Shen<sup>b</sup>

<sup>a</sup> School of Aerospace, Mechanical and Mechatronic Engineering, The University of Sydney, Sydney, NSW 2006, Australia

<sup>b</sup> State Key Laboratory of Advanced Welding and Joining, Harbin Institute of Technology, Harbin 150001, China

<sup>c</sup> Departments of Aerospace & Mechanical Engineering and Materials Science, University of Southern California, Los Angeles, CA 90089-1453, USA

<sup>d</sup> Australian Centre of Microscopy and Microanalysis, The University of Sydney, Sydney, NSW 2006, Australia

<sup>e</sup> Center for Advancing Materials Performance from the Nanoscale (CAMP-Nano) and Hysitron Applied Research Centre in China (HARCC), State Key Laboratory for Mechanical Behavior of Materials, Xi'an Jiaotong University, Xi'an 710049, China

<sup>f</sup> Materials Research Group, School of Engineering Sciences, University of Southampton, Southampton SO17 1BJ, UK

Received 7 September 2011; accepted 19 September 2011

Available online 29 October 2011

## Abstract

The great technological potential for bulk metallic glasses (BMGs) arises primarily because of their superior mechanical properties. To realize this potential, it is essential to overcome the severe ductility limitations of BMGs which are generally attributed to shear localization and strain softening. Despite much international effort, progress in improving the ductility of BMGs has been limited to certain alloys with specific compositions. Here, we report that severe plastic deformation of a quasi-constrained volume, which prevents brittle materials from fracture during the plastic deformation, can be used to induce strain hardening and to reduce shear localization in BMGs, thereby giving a significant enhancement in their ductility. Structural characterizations reveal the increased free volume and nanoscale heterogeneity induced by severe plastic deformation are responsible for the improved ductility. This finding opens a new and important pathway towards enhanced ductility of BMGs.

© 2011 Acta Materialia Inc. Published by Elsevier Ltd. All rights reserved.

**Keywords:** Bulk metallic glasses; Ductility; Severe plastic deformation; Transmission electron microscopy

## 1. Introduction

Bulk metallic glasses (BMGs) have significant potential for technological applications due to their superior mechanical properties, including high elastic limit (up to 2%), super high strength (~2 GPa) and hardness, and excellent resistance to wear and corrosion [1–4]. However, practical structural applications of BMGs are severely limited by their poor ductility, which is usually near zero in tension and less than 2% under compression [2–5]. The

poor ductility of BMGs is caused by shear localization and strain/thermal softening [2,4,6,7]. Through significant global efforts, two general methods have been proposed to enhance the ductility of BMGs: (1) fabrication of amorphous/crystalline composite structures [8–12] and (2) design of BMGs with specific compositions [7,13–15]. However, these methods apply only to certain specific BMGs. The second method is particularly sensitive to BMG composition and slight deviations in stoichiometry can lead to dramatic ductile-to-brittle transitions [13,16]. Here, we report that severe plastic deformation (SPD), which has been widely used to manipulate the structures of crystalline materials to achieve enhanced mechanical properties [17,18], can be used also to modify the micro-

\* Corresponding author. Tel.: +61 2 93512348; fax: +61 2 9351 7060.

E-mail address: [xiaozhou.liao@sydney.edu.au](mailto:xiaozhou.liao@sydney.edu.au) (X.Z. Liao).

structures of BMGs by increasing their free volume and inducing microstructural heterogeneity at the nanoscale through deformation-induced atomic clustering processes. These microstructures effectively reduce shear localization and induce a strain hardening capability leading to a significant enhancement in their ductility.

## 2. Experimental procedures

The BMG studied here was  $Zr_{50.7}Cu_{28}Ni_9Al_{12.3}$  (at.%), which was prepared by first arc melting the pure elements Zr (99.9%), Cu (99.99%), Ni (99.9%), and Al (99.99%) three times in a Ti-gettered argon atmosphere to form the master ingot based on the nominated composition. The ingot was then remelted and drop-cast into a copper mold to obtain an amorphous plate with dimensions of 60 mm × 30 mm × 3 mm.

SPD processing was conducted on BMG disks using high-pressure torsion (HPT) under quasi-constrained conditions [17,19] in which a BMG disk was held to a fixed volume to prevent fracturing of the brittle BMG during the SPD processing. The BMG was cut into disks with diameters of ~10 mm and thicknesses of ~0.8 mm. The disks were subjected to HPT under a pressure of 6 GPa at room temperature for 1 and 2 revolutions, respectively. The rotation speed of HPT processing was 1 rev min<sup>-1</sup>. After HPT processing, the disks were mechanically polished to produce a mirror-like surface using diamond lapping films (30–1 μm) for X-ray diffraction (XRD) measurements and hardness testing. XRD measurements were performed using a Siemens D5000 diffractometer. Hardness testing was carried out using a Leco LV700AT indenter with loads of 10 and 30 kg, respectively, at each point for 15 s. The hardness was measured at points with radius values on the HPT disks of  $r = 1.0, 1.7, 2.4, 3.1$  and 3.8 mm and these values were averaged from eight datum points positioned by a rotational increment of 45° around the disk center. The hardness value at the disk central area ( $r = 0.3$  mm) was averaged from three datum points by a rotational increment of 120° around the disk center. The indented areas were characterized by scanning electron microscopy (SEM) using a Zeiss ULTRA microscope.

Thermal analysis was performed using DSC 2920 under pure nitrogen atmosphere with a heating rate of 20 °C min<sup>-1</sup>.  $Zr_{50.7}Cu_{28}Ni_9Al_{12.3}$  (at.%) metallic glass samples were put into Al pans at room temperature for 1 min, and then heated to 850 K. Each sample was run for two times and the second measured data for a fully crystallized sample is used as base line. The difference between the two measurements is the real heat flow change for the sample. It has been confirmed that free volume change is related to the enthalpy change of samples. Their relationship can be expressed using the following equation [20]:

$$\Delta H_i = \beta \cdot \Delta V_i$$

where  $\Delta H_i$  is the change of enthalpy,  $\beta$  is a constant and  $\Delta V_i$  is the change of free volume. The difference of total

enthalpy  $\Delta H_i$  for each specimen caused by structural change induced by HPT is calculated as follows [21]:

$$\Delta H_i = \int_{375K}^{700K} \frac{W_i^{exp}(T) - W_i^{base}(T)}{c} dT - \int_{375K}^{700K} \frac{W_0^{exp}(T) - W_0^{base}(T)}{c} dT$$

where  $W^{exp}(T)$  and  $W^{base}(T)$  is the heat flow of the experiment and base line, respectively;  $i$  corresponds to data for the BMG after HPT, 0 corresponds to data for the as-received sample; and  $c$  is the heating rate (20 °C min<sup>-1</sup>). The total enthalpy change should be integrated from 375 K to the glass transition temperature (700 K) to reveal the change of free volume. Compared to the as-received sample, the enthalpy change of the HPT-deformed sample (the center of the one-revolution disk) is 1.8 J g<sup>-1</sup> which demonstrates HPT induces an increase of free volume.

Pillars for in situ compression transmission electron microscope (TEM) were prepared using a FEI Helios Nanolab 600 focused ion beam (FIB). High-resolution TEM images of BMGs were taken using a JEM-3000F TEM. In situ compression testing of the BMG was conducted using a Hysitron PicoIndenter [22] with a flat diamond punch in a JEM-2100 TEM. The load and spatial resolutions of the PicoIndenter are ~0.3 mN and ~1 nm, respectively. Deformation processes in TEM were recorded at 30 frames s<sup>-1</sup> using a digital video recorder in the microscope.

## 3. Results

Fig. 1 shows the hardness of the as-cast and HPT BMG as a function of the distance from the central area of each

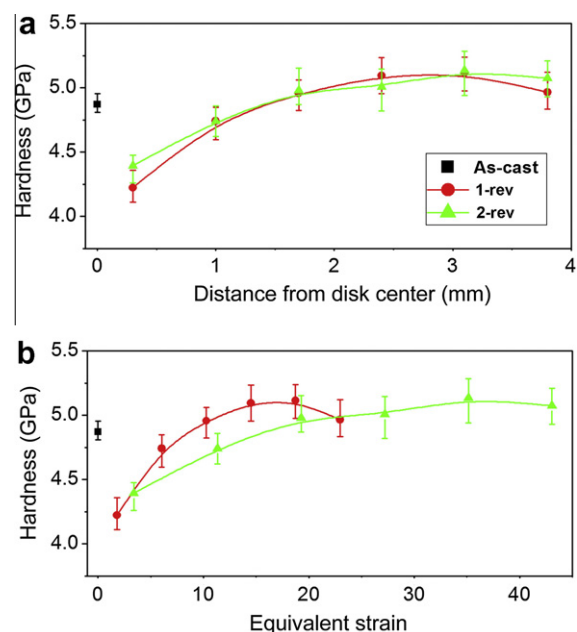


Fig. 1. The hardness of the as-cast and HPT BMG as a function of (a) distance from each disk center and (b) von Mises equivalent strain.

disk (Fig. 1a) and as a function of the von Mises equivalent strain [23] (Fig. 1b) applied by the HPT processing. The hardness testing results clearly indicate that strain softening occurred, resulting in a  $\sim 13\%$  drop in hardness from  $\sim 4.8$  GPa in the as-cast sample to  $\sim 4.2$  GPa at the central area of the one-revolution HPT disk. Because the torsional plastic strain is close to zero at the central area of a one-revolution HPT disk [24], it is reasonable to conclude that the strain softening process occurred immediately after a high pressure of 6 GPa was applied to the BMG but before torsional straining. Substantial ( $\sim 19\%$ ) strain hardening was subsequently observed in the early stages of the HPT straining before the hardness reached a plateau of  $\sim 5$  GPa at an equivalent strain of  $\sim 40$ .

While strain softening is commonly observed in BMGs, and usually associated with their poor ductility, strain hardening is rare [8,25,26]. To understand the deformation behavior related to strain softening and strain hardening, SEM observation was conducted at indented areas in the as-cast sample and in the central area of the one-revolution HPT disk. All indents were of a regular pyramidal shape (Fig. 2). It is interesting to note that, under 10 kg loading, obvious shear bands (SBs) with spacing of  $\sim 10$   $\mu\text{m}$  or more are seen near the indented area in the as-cast sample (Fig. 2a and b) where strain softening occurred upon indentation. However, no clear SB was observed in the surrounding area of each indent in the center of the one-revolution HPT sample (Fig. 2c and d) in which strain hardening took place during the indentation. The existence of a low density of coarse SBs in the as-cast sample is strong evidence of shear localization. The lack of SBs in the center of the one-revolution HPT sample indicates that HPT processing eliminates or significantly reduces shear localization, thereby giving a more uniform deformation. By increasing the indentation loading to 30 kg, a low density of continuous coarse SBs remained in the as-cast sample (Fig. 2e), and a very high density of short shallow SBs was present in the center of the one-revolution HPT sample (Fig. 2f), further confirming the reduction of shear localization after HPT processing.

The introduction of a strain-hardening capacity and the reduction of shear localization in HPT samples indicate that HPT represents a strategy to enhance the ductility of BMGs. To confirm this, extensive in situ compression experiments of pillars with rectangular-shaped cross-sections and without tapering were conducted using TEM. The simple pillar geometry eliminates the complicated effects on mechanical properties that are caused by tapering [22,26,28]. In situ compression of five pillars fabricated from the as-cast sample indicated that the as-cast BMG is brittle with small plastic strain. Fig. 3 shows a typical example of the compression of a pillar from the as-cast sample. The pillar shown in Fig. 3a possessed dimensions of 303 nm (width)  $\times$  278 nm (thickness)  $\times$  469 nm (length). In situ TEM compression was carried out under the displacement-controlled mode with a nominal strain rate of

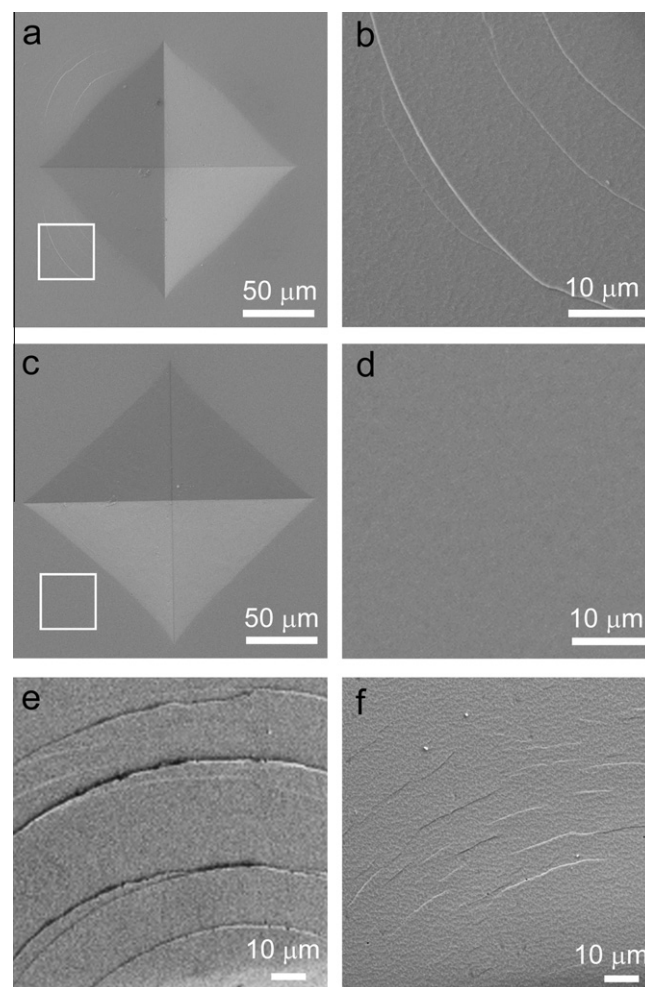


Fig. 2. SEM images of (a) an indented area of the as-cast sample under 10 kg loading, (b) an enlarged image of the region marked with a white square in (a), (c) an indented area of the HPT disk under 10 kg loading, (d) an enlarged image of the region marked with a white square in (c), (e) SB morphology at an area close to an indent on the as-cast sample under 30 kg loading, and (f) SB morphology at an area close to an indent on the HPT disk under 30 kg loading.

$\sim 10^{-2} \text{ s}^{-1}$ . An engineering stress–strain curve (Fig. 3b) shows that the stress increased linearly to  $\sim 2.8$  GPa before yielding and dropped rapidly to zero at a plastic strain of  $\sim 1.5\%$ , which is typical behavior of brittle BMGs [5]. Note that the elastic strain obtained from Fig. 3b is overestimated because of the gliding of the TEM sample on the specimen mount in the early stages of the compression testing, as demonstrated by the corresponding video (Movie 1) in the online Supplementary information. Together with the in situ experiment shown in Movie 1, a post-deformation SEM observation (Fig. 3c) confirmed that the pillar fractured instantaneously via the motion of a single SB.

By contrast, in situ compression of three pillars fabricated from the central region of the one-revolution HPT sample showed excellent ductility. A typical example is shown in Fig. 4. A pillar with dimensions of 321 nm  $\times$  343 nm  $\times$  667 nm (Fig. 4a) was compressed under the same experimental setting as in Fig. 3. An

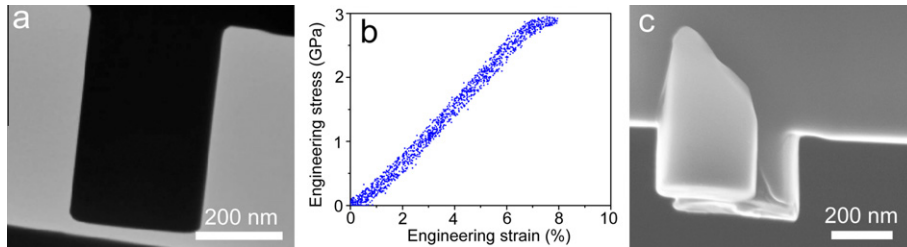


Fig. 3. (a) A pillar of the as-cast sample before compression, (b) an engineering stress–strain curve of the compression test, and (c) an SEM image of the pillar after compression, showing a brittle fracture along a single SB.

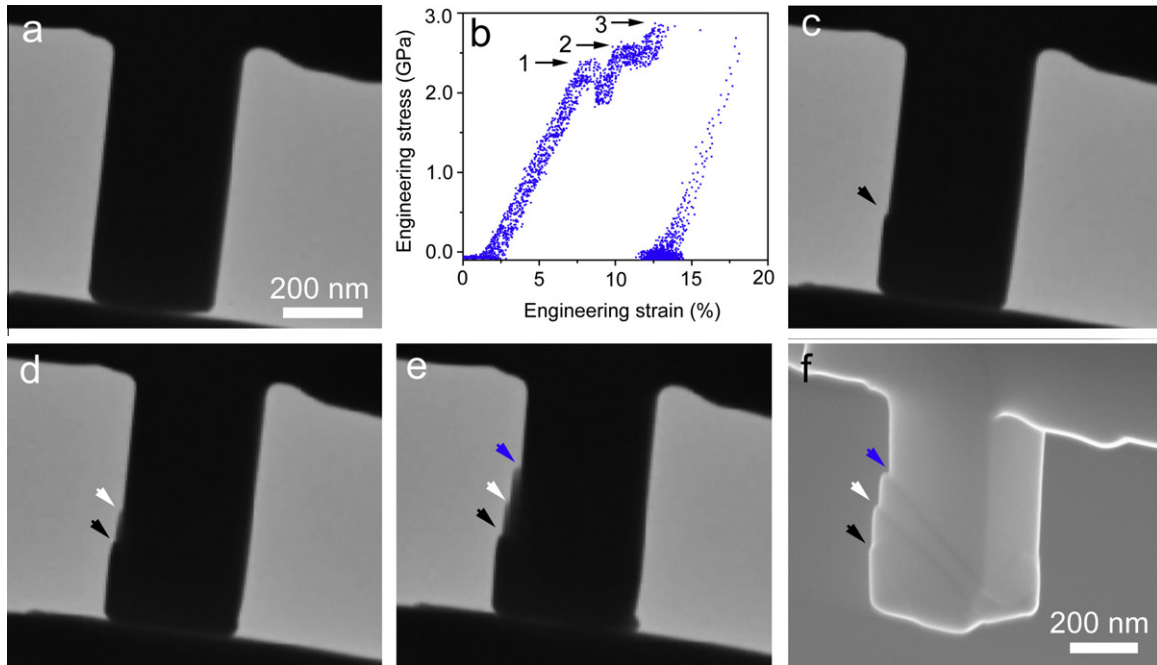


Fig. 4. (a) A pillar of the HPT deformed sample before in situ compression, (b) an engineering stress–strain curve for the HPT deformed sample, indicating strain hardening. (c–e) are extracted TEM images corresponding to point 1–3 in (b), respectively, and (f) an SEM image after the compression.

engineering stress–strain curve is presented in Fig. 4b in which points 1–3 correspond to the morphological images in Fig. 4c–e, respectively, which are extracted from Movie 2 (see the online Supplementary information). The pillar yielded at a stress of  $\sim 2.3$  GPa (marked as point 1 in Fig. 4b), which is  $\sim 18\%$  lower than 2.8 GPa in the as-cast sample, through the activation of a SB marked with a black arrow in Fig. 4c. The stress decreased because of the SB initiation. Increasing deformation resulted in strain hardening, indicating that the SB was blocked. Subsequent deformation resulted in the initiation of a second SB (marked with a white arrow in Fig. 4d) at the stress level of 2.5 GPa (marked as point 2 in Fig. 4b). Slight propagation of the second SB occurred, followed by further strain hardening to a stress of 2.8 GPa (marked as point 3 in Fig. 4b) when the third SB was activated (indicated with a blue arrow above the white arrow in Fig. 4e). The compression stopped at this point without breaking the pillar and the punch was withdrawn. The post-deformation SEM image in Fig. 4f shows clearly the three SBs with

no indication of fracture. The small spacing between neighboring SBs agrees well with the observed high density of SBs surrounding an indent on the surface of the HPT sample as shown in Fig. 2. The engineering strain of the pillar in Fig. 4 reached 11% but the integrity of the pillar was maintained.

It should be noted that the strain hardening shown in the engineering stress–strain curve in Fig. 4b is real. Although the cross-sectional area at the tip of the pillar increased with the compressive strain, the cross-sectional areas at places where SB deformation occurred remained roughly unchanged at the time when the deformation was initiated. It has been widely reported that reducing the dimensions of BMGs to smaller than 100 nm increases significantly the ductility of these materials [26,29,30]. The dimensions of the pillars investigated here are much larger than 100 nm. Furthermore, with similar dimensions, as-cast pillars and HPT pillars behave differently and consistently. Therefore, the observed high ductility in HPT pillars is confirmed as a real property of the HPT BMG.

In fact, plastic strain much larger than 11% was observed in pillars fabricated from the central area of the one-revolution HPT disk when these pillars were compressed to fracture. Fig. 5 shows three consecutive compression processes of a pillar with dimensions of  $313 \text{ nm} \times 313 \text{ nm} \times 450 \text{ nm}$  (Fig. 5a) fabricated from the central region of the one-revolution HPT sample. The pillar was compressed with a nominal strain rate of  $\sim 10^{-2} \text{ s}^{-1}$ . Several loading peaks were present in the load–time curves in Fig. 5b. Fig. 5c–e shows microstructural images extracted from Movies 3.1–3.3 after the first, second and third loading test, respectively. During test 1, the load increased rapidly to  $233 \mu\text{N}$  (point 1 in Fig. 5b) followed by the formation of a SB, which is marked by a black arrowhead in Fig. 5c, and a load drop to  $86 \mu\text{N}$ . Continuing the compression to the load of  $160 \mu\text{N}$  (point 2 in Fig. 5b) before the end of the first loading cycle only resulted in elastic deformation and the deformation was gradually released when the punch used to apply the compression load was withdrawn (Movie 3.1). During test 2, the previous SB was activated again at a higher load of  $\sim 260 \mu\text{N}$  (point 3 in Fig. 5b), resulting in another load drop. The higher loading needed to activate the same SB indicates that the SB was blocked or arrested by an obstacle that resulted in strain hardening. The SB propagated only a short distance before it was arrested again, as evidenced by the immediate increase of the applied force. Before the end of the loading cycle 2, the second SB (marked with a red arrow in Fig. 5d) was activated at  $\sim 280 \mu\text{N}$  (point 4 in Fig. 5b) that separated the punch and the pillar (because the pillar receded faster than the punch), leading to a rapid load drop to zero (Movie 3.2).

During test 3, the second SB continued to propagate when the force reached  $\sim 300 \mu\text{N}$  (point 5 in Fig. 5b) but was immediately arrested. The third SB was activated at  $\sim 315 \mu\text{N}$  (point 6 in Fig. 5b) that led to the fracture of the pillar (Fig. 5e and f and Movie 3.3). The accumulated engineering strain of the three compression processes is about 52%, from the expression  $\frac{L_0 - L_3}{L_0}$  ( $L_0 = 450 \text{ nm}$  and  $L_3 = 217 \text{ nm}$ ).

To understand the microstructural factors that enhance the ductility, extensive microstructural characterizations were carried out using X-ray diffractometry (XRD), differential scanning calorimetry (DSC), electron diffraction and high-resolution TEM. Fig. 6a provides the XRD patterns of samples before and after HPT processing. The two patterns exhibit almost identical shapes, indicating that the microstructures remained mainly in an amorphous state with no XRD detectable crystallization after HPT. The DSC traces in Fig. 6b further confirm the glassy state with a glass transition temperature evident at  $700 \text{ K}$  for both samples. The DSC data also suggest that the energy release increased from  $2.0 \text{ J g}^{-1}$  in the as-cast sample to  $3.8 \text{ J g}^{-1}$  in the central region of the one-revolution HPT sample, so that the free volume increases after HPT. It is generally accepted that plastic deformation of BMGs, including by SPD processing, requires dilatation that produces geometric defects with a low packing density so that excess volumes are created [16,31–33]. This explains that SPD processing increased the free volume in the present BMG.

Fig. 7a shows a typical bright-field TEM image and its corresponding electron diffraction pattern (inserted at the upper right corner) recorded from the as-cast BMG. The uniform image contrast and electron diffraction rings in

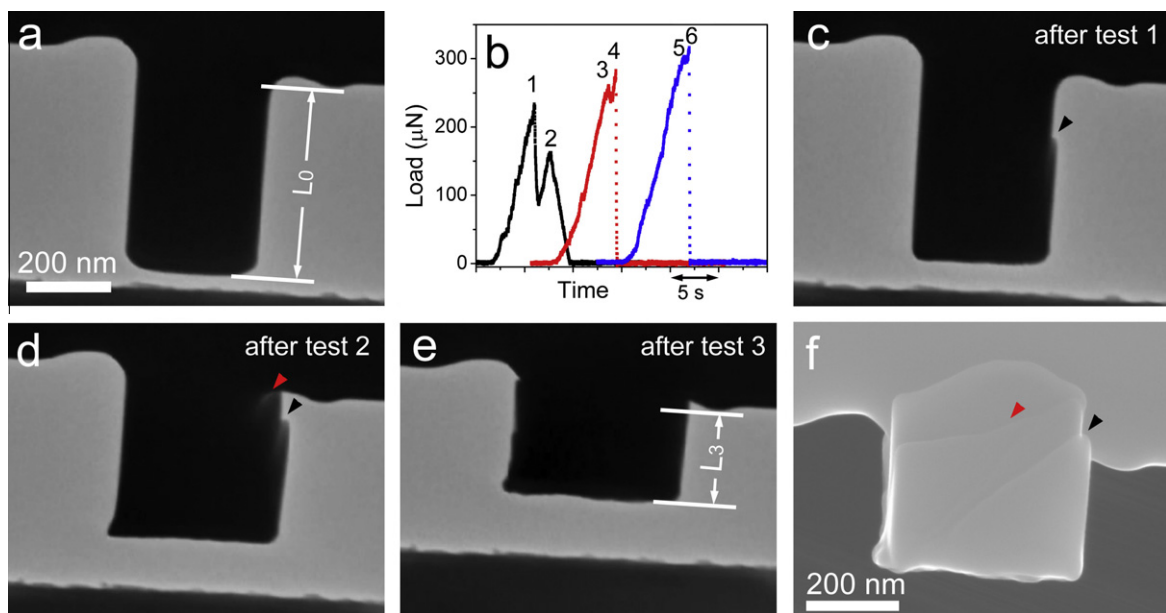


Fig. 5. Three consecutive compression tests on a pillar at the central region of the one-revolution HPT disk. (a) The pillar before compression, (b) load–time curves for test 1 (the black curve), test 2 (the red curve) and test 3 (the blue curve), (c–e) still images after each test extracted from the video Movies 3.1–3.3 of the in situ compression tests, and (f) an SEM image after test 3. (For interpretation of the references to colour in this figure legend, the reader is referred to the web version of this article.)

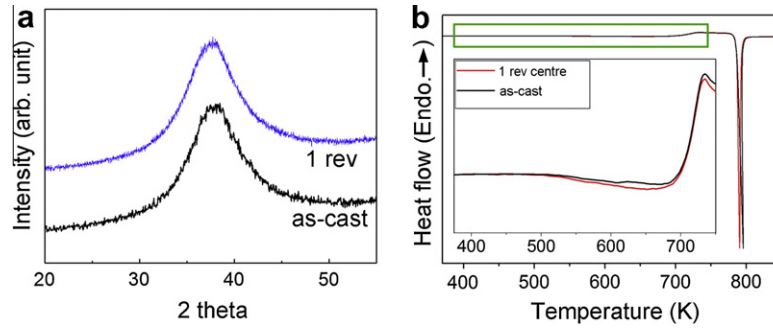


Fig. 6. (a) XRD patterns and (b) DSC traces of the as-cast and HPT samples.

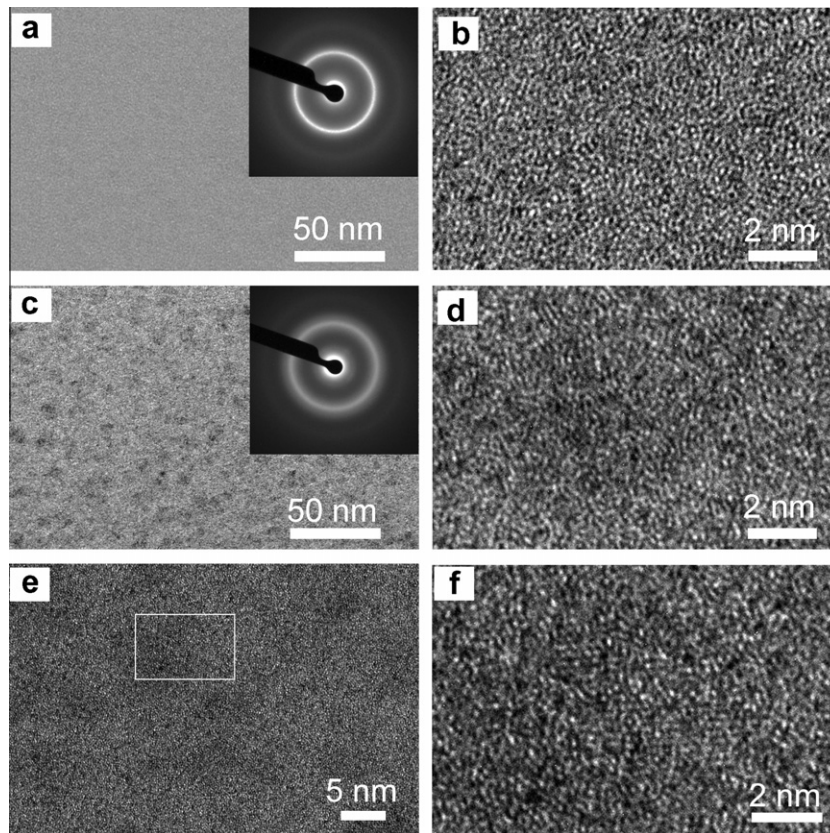


Fig. 7. (a and b) A typical bright-field TEM image with an insert diffraction pattern and a high-resolution TEM image, respectively, of the as-cast sample; (c and d) a typical bright-field TEM image with an insert diffraction pattern and a high-resolution TEM image, respectively, of the central area of the one-revolution HPT disk; (e) a high-resolution TEM image obtained from the central area of the one-revolution HPT disk showing partial crystallization of a small dark region; (f) an enlarged image of the rectangle area in (e).

Fig. 7a as well as the high-resolution TEM image in Fig. 7b reveal a typical uniform amorphous structure in the as-cast BMG. Fig. 7c shows a typical bright-field TEM image recorded from the central region of the one-revolution HPT BMG, demonstrating a high density of dark contrast regions with diameters of  $\sim 5$  nm distributed uniformly throughout the sample. The bright/dark contrast variation in Fig. 7c indicates a nanoscale microstructural heterogeneity in the material, which may be caused by chemical short-range segregation [34–36]. The insert electron diffraction pattern in Fig. 7c and the high-resolution TEM image in Fig. 7d confirm that the HPT sample retained mainly an amorphous structure. Note that a fraction of these dark

regions was partially crystallized. Fig. 7e shows a typical image of partial crystallization of a dark region at the central area of the one-revolution HPT sample. An area in Fig. 7e highlighted with a white rectangle is magnified in Fig. 7f, showing a few horizontal crystal lattice fringes. These results demonstrate that processing by HPT produces a structural change that forms a high density of nanoscale heterogeneity regions distributed uniformly throughout the BMG. These deformation-induced microstructural inhomogeneities operate over a length scale of several nanometers and are probably caused by the thermodynamic metastability intrinsic to metallic glasses [37–40].

#### 4. Discussion

Owing to the absence of dislocation-mediated crystallographic slip, BMGs usually exhibit localized shear deformation via shear banding that initiates strain softening upon yielding [7,14,16,31,40–42]. This makes BMGs very brittle such that they fail catastrophically due to the uninhibited propagation of SBs [2,4,5,7,26]. To improve the ductility of BMGs, it is necessary: (1) to promote the generation of a large number of SBs so that the macroscopic strain is distributed over a large volume; and (2) to produce strain hardening in order to impede SB propagation and thereby reduce the strain within a single SB, thus delaying fracture [4,7,14,15].

Because the mechanical coupling in free volume sites is weak, these sites may be the preferred regions for SB nucleation under an applied stress [3,16,31,43]. Processing by SPD introduces an excessive free volume that provides numerous SB sources and thereby effectively distributes the plastic deformation over a large volume. Other defects introduced by HPT processing may also be preferred SB nucleation sites. While significantly increasing the number of SB nucleation sites prevents localized deformation, it also leads to a softening because of the easy initiation of shear banding deformation. This is probably the reason for the reduction in hardness from  $\sim 4.8$  GPa in the as-cast BMG to  $\sim 4.2$  GPa immediately after a compressive force of 6 GPa was applied to the BMG at the beginning of the HPT processing.

While the easy nucleation of SBs is an essential factor for inherent ductility, strain hardening is necessary to allow these materials to sustain plastic strain by preventing runaway failure along a single SB. Studies revealed that sub-nanometer-scale structural inhomogeneity not only promotes the nucleation of SBs but also enables their branching, leading to a large global plasticity [8,35]. It has been suggested that in situ nanocrystallization along SBs during the deformation process can dramatically increase the strength of the shear regions [9] and this may effectively compensate for the strain softening [9,25]. The nanoscale heterogeneous regions presented in Fig. 7c should play a similar role in hindering, deflecting and branching the propagation of SBs, resulting in discontinuity of the SBs, as shown in Fig. 2f. By contrast, deformation in the as-cast sample was associated with the continuous propagation of long and coarse SBs (see Fig. 2e), leading to catastrophic failure. This explains our observation in the HPT BMG that SBs were arrested during in situ compression and a higher stress is needed to activate new SBs. During deformation, SB initiation will start from the weakest sites. With further deformation, the critical stresses to initiate new SBs increase gradually from easy to difficult nucleation sites, resulting in a progressive increase of stress needed to sustain further deformation. This means that strain hardening will occur. Note that the reactivation of previous SBs also requires a higher stress, which was demonstrated by in situ

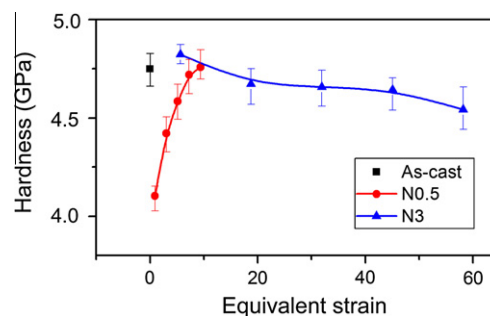


Fig. 8. The hardness of the as-cast and HPT  $\text{Ti}_{40}\text{Zr}_{25}\text{Ni}_3\text{Cu}_{12}\text{Be}_{20}$  (at.%) BMG as a function of the von Mises equivalent strain. N0.5 and N3 represent 0.5 and 3 HPT revolutions, respectively.

deformation TEM (see Fig. 5 and Movies 3.1–3.3 in Supplementary information). These results confirm that strain hardening is an intrinsic property of severely deformed BMGs. The mechanisms of the ductility enhancement in HPT BMGs are different from that of a shot-peened BMG where the introduction of a large amount of pre-existing SBs enhanced the plasticity of the BMG [44]. No pre-existing SBs were observed in the HPT BMGs used in this study.

It has been reported that thermal annealing can also be used to introduce structural heterogeneity (such as nanocrystals) as an approach to improve ductility, although the improvement derived from these approaches is rather limited [45]. Further, thermal annealing can result in a complete loss in ductility in some metallic glasses [46]. By comparison, SPD is a more promising technique for the introduction of microstructural heterogeneity in BMGs. Because a deformation-induced free volume increase [47–49] and deformation-induced nanocrystallization [37,40] have been widely reported in BMGs with various compositions, the method reported here, whereby a strain hardening capability is introduced to improve the ductility of BMGs, should have a generality for BMGs with various compositions. To confirm this possibility, HPT processing followed by hardness testing was carried out on a  $\text{Ti}_{40}\text{Zr}_{25}\text{Ni}_3\text{Cu}_{12}\text{Be}_{20}$  (at.%) BMG and the results of strain hardening are shown in Fig. 8.

#### 5. Conclusions

In summary, we propose a universal technique to improve significantly the ductility of BMGs by using SPD processing of a quasi-constrained volume as in high-pressure torsion. The use of a quasi-constrained volume effectively prevents brittle BMGs from fracture during the plastic deformation process. The processing introduces an excessive free volume and nanoscale microstructural heterogeneity in BMGs that enable mechanisms for the enhanced ductility of BMGs. The results offer a new paradigm for developing BMGs with improved ductility and this will have a significant impact on the research and applications of BMGs.

## Acknowledgements

The authors are grateful for the scientific and technical input and support from the Australian Microscopy & Microanalysis Research Facility node at the University of Sydney. This research was financially supported by the Australian Research Council. MK and TGL were supported by the National Science Foundation of the United States under Grant No. DMR-0855009 and by the European Research Council under ERC Grant Agreement No. 267464-SPD-METALS. ZWS was supported by NSFC (50925104) and the 973 program of China (2010CB631003).

## Appendix A. Supplementary material

Supplementary data associated with this article can be found, in the online version, at [doi:10.1016/j.actamat.2011.09.026](https://doi.org/10.1016/j.actamat.2011.09.026).

## References

- [1] Inoue A. *Acta Mater* 2000;48:279.
- [2] Trexler MM, Thadhani NN. *Prog Mater Sci* 2010;55:759.
- [3] Johnson WL. *Mater Res Soc Bull* 1999;24:42.
- [4] Schuh C, Hufnagel T, Ramamurty U. *Acta Mater* 2007;55:4067.
- [5] Zhang ZF, Eckert J, Schultz L. *Acta Mater* 2003;51:1167.
- [6] Lewandowski JJ, Greer AL. *Nature Mater* 2006;5:15.
- [7] Xing LQ, Li Y, Ramesh KT, Li J, Hufnagel TC. *Phys Rev B* 2001;64:180201.
- [8] Das J, Tang MB, Kim KB, Theissmann R, Baier F, Wang WH, et al. *Phys Rev Lett* 2005;94:205501.
- [9] Chen MW, Inoue A, Zhang W, Sakurai T. *Phys Rev Lett* 2006;96:245502.
- [10] Fan C, Ott RT, Hufnagel TC. *Appl Phys Lett* 2002;81:1020.
- [11] Hofmann DC, Suh JY, Wiest A, Duan G, Lind ML, Demetriou MD, et al. *Nature* 2008;451:1085.
- [12] Eckert J, Das J, Pauly S, Duhamel C. *J Mater Res* 2007;22:285.
- [13] Liu YH, Wang G, Wang RJ, Zhao DQ, Pan MX, Wang WH. *Science* 2007;315:1385.
- [14] Bei H, Xie S, George EP. *Phys Rev Lett* 2006;96:105503.
- [15] Schroers J, Johnson WL. *Phys Rev Lett* 2004;93:255506.
- [16] Chen MW. *Annu Rev Mater Res* 2008;38:445.
- [17] Zhilyaev AP, Langdon TG. *Prog Mater Sci* 2008;53:893.
- [18] Liddicoat PV, Liao XZ, Zhao YH, Zhu YT, Murashkin MY, Lavernia EJ, et al. *Nature Commun* 2010;1:63.
- [19] Figueiredo RB, Cetlin PR, Langdon TG. *Mater Sci Eng A* 2011;528:8198.
- [20] Van Den Beukel A, Sietsma J. *Acta Metal Mater* 1990;38:383.
- [21] Slipenyuk A, Eckert J. *Scripta Mater* 2004;50:39.
- [22] Shan ZW, Li J, Cheng YQ, Minor AM, Asif SAS, Warren OL, et al. *Phys Rev B* 2008;77:155419.
- [23] Edalati K, Horita Z. *Mater Trans* 2010;51:1051.
- [24] Cao Y, Wang YB, Figueiredo RB, Chang L, Liao XZ, Kawasaki M, et al. *Acta Mater* 2011;59:3903.
- [25] Wang K, Fujita T, Zeng YQ, Nishiyama N, Inoue A, Chen MW. *Acta Mater* 2008;56:2834.
- [26] Jang DC, Greer JR. *Nature Mater* 2010;9:215.
- [27] Uchic MD, Dimiduk DM, Florando JN, Nix WD. *Science* 2004;305:986.
- [28] Schuster BE, Wei Q, Hufnagel TC, Ramesh KT. *Acta Mater* 2008;56:5091.
- [29] Guo H, Yan PF, Wang YB, Tan J, Zhang ZF, Sui ML, et al. *Nature Mater* 2007;6:735.
- [30] Luo JH, Wu FF, Huang JY, Wang JQ, Mao SX. *Phys Rev Lett* 2010;104:215503.
- [31] Spaepen F. *Acta Metal* 1977;25:407.
- [32] Spaepen F. *Nature Mater* 2006;5:7.
- [33] Wang XD, Cao QP, Jiang JZ, Franz H, Schroers J, Valiev RZ, et al. *Scripta Mater* 2011;64:81.
- [34] Fujita T, Konno K, Zhang W, Kumar V, Matsuura M, Inoue A, et al. *Phys Rev Lett* 2009;103:075502.
- [35] Liu YH, Wang D, Nakajima K, Zhang W, Hirata A, Nishi T, et al. *Phys Rev Lett* 2011;106:125504.
- [36] Asoka-Kuma P, Hartley J, Howell R, Sterene PA, Nieh TG. *Appl Phys Lett* 2000;77:1973.
- [37] Kim JJ, Choi Y, Suresh S, Argon AS. *Science* 2002;295:654.
- [38] Wang G, Liu YH, Yu P, Zhao DQ, Pan MX, Wang WH. *Appl Phys Lett* 2006;89:251909.
- [39] Lee SW, Huh MY, Fleury E, Lee JC. *Acta Mater* 2006;54:349.
- [40] Chen H, He Y, Shiflet GJ, Poon SJ. *Nature* 1994;367:541.
- [41] Stief PS, Spaepen F, Hutchinson JW. *Acta Metall* 1982;30:447.
- [42] Flores KM, Dauskardt RH. *J Mater Res* 1999;14:638.
- [43] Argon AS. *Acta Metal* 1979;27:47.
- [44] Zhang Y, Wang WH, Greer AL. *Nature Mater* 2006;5:857.
- [45] Chen MW, Inoue A, Fan C, Sakai A, Sakurai T. *Appl Phys Lett* 1999;74:2131.
- [46] Murali P, Ramamurty U. *Acta Mater* 2005;53:1467.
- [47] Hajlaoui K, Benameur T, Vaughan G, Yavari AR. *Scripta Mater* 2004;51:843.
- [48] Flores KM, Suh D, Dauskardt RH, Asoka-Kumar P, Sterne PA, Howell RH. *J Mater Res* 2002;17:1153.
- [49] Bhowmick R, Raghavan R, Chattopadhyay K, Ramamurty U. *Acta Mater* 2006;54:4221.